MIT Libraries | DSpace@MIT

MIT Open Access Articles

Encoding of vinylidene isomerization in its anion photoelectron spectrum

The MIT Faculty has made this article openly available. ***Please share*** how this access benefits you. Your story matters.

Citation: DeVine, Jessalyn A. et al. "Encoding of vinylidene isomerization in its anion photoelectron spectrum." Science 358, 6361 (October 2017): 336-339 © 2017 The Authors

As Published: http://dx.doi.org/10.1126/science.aao1905

Publisher: American Association for the Advancement of Science (AAAS)

Persistent URL: http://hdl.handle.net/1721.1/115219

Version: Author's final manuscript: final author's manuscript post peer review, without publisher's formatting or copy editing

Terms of use: Creative Commons Attribution-Noncommercial-Share Alike

Massachusetts Institute of Technology

Title: Encoding of vinylidene isomerization in its anion photoelectron spectrum

Authors: Jessalyn A. DeVine,[1,†] Marissa L. Weichman,[1,†] Benjamin Laws,[2] Jing Chang,[3] Mark C. Babin,[1] Garikoitz Balerdi,[4] Changjian Xie,[5] Christopher L. Malbon,[6] W. Carl Lineberger,[7] David R. Yarkony,[6] Robert W. Field,[8] Stephen T. Gibson,[2] Jianyi Ma,[3,*] Hua Guo,[5] Daniel M. Neumark[1,9,*]

Affiliations:

[1]Department of Chemistry, University of California, Berkeley, California 94720, United States.

[2]Research School of Physics and Engineering, Australian National University, Canberra, ACT 2601, Australia.

[3]Institute of Atomic and Molecular Physics, Sichuan University, Chengdu, Sichuan 610067, China.

[4]Departmento de Química Física, Facultad de Ciencias Químicas, Universidad Complutense de Madrid (Unidad Asociada I+D+I CSIC), 28040 Madrid, Spain.

[5]Department of Chemistry and Chemical Biology, University of New Mexico, Albuquerque, New Mexico 87131, United States.

[6]Department of Chemistry, Johns Hopkins University, Baltimore, Maryland 21218, United States.

[7]JILA and Department of Chemistry and Biochemistry, University of Colorado, Boulder, Colorado 80309, United States.

[8]Department of Chemistry, Massachusetts Institute of Technology, Cambridge, Massachusetts 02139, United States.

[9]Chemical Sciences Division, Lawrence Berkeley National Laboratory, Berkeley, California 94720, United States.

*Correspondence to: majianyi81@163.com, dneumark@berkeley.edu

†These authors contributed equally to this work.

Abstract: Vinylidene-acetylene isomerization is the prototypical example of a 1,2-hydrogen shift, one of the most important classes of isomerization reactions in organic chemistry. This reaction was investigated with quantum state specificity by high-resolution photoelectron spectroscopy of the H_2CC^- and D_2CC^- anions and quantum dynamics calculations. Peaks in the photoelectron spectra are considerably narrower than in previous work and reveal subtleties in the isomerization dynamics of neutral vinylidene, as well as vibronic coupling with an excited state of vinylidene. Comparison with theory permits assignment of most spectral features to eigenstates dominated by vinylidene character. However, excitation of the ν_6 in-plane rocking mode in H_2CC leads to appreciable tunneling-facilitated mixing with highly vibrationally-excited states of acetylene, leading to broadening and/or spectral fine structure that is largely suppressed for analogous vibrational levels of D_2CC.

One Sentence Summary: Experiment and theory are combined to reveal the quantum state-specific dynamics of the 1,2-hydrogen shift from vinylidene to acetylene, the prototype of one the most important isomerization mechanisms in organic chemistry.

Main Text: The 1,2-hydrogen shift is the simplest bond-breaking isomerization reaction in organic chemistry (*1*), and the prototypical example of this process is the isomerization of vinylidene (H_2CC) to acetylene (HCCH). Vinylidene, the smallest unsaturated carbene (*2*), has been implicated as a transient intermediate in many chemical processes (*3*-*6*), but is of particular interest as a high-energy form of acetylene (*7*). From the perspective of chemical physics, the $H_2CC \rightleftharpoons$HCCH isomerization (Fig. 1) is a benchmark unimolecular reaction; the small number of atoms allows application of sophisticated theoretical methods to describe the isomerization dynamics (*8*-*13*), and the interplay between theory and experiment has provided a great deal of insight into this reaction (*14*, *15*). The low barrier (~0.1 eV, see Figure 1) for vinylidene isomerization (*8*, *10*) is responsible for extensive tunneling interactions with acetylene states, and over the past several decades considerable effort has been invested in probing this isomerization from both sides of the barrier. On the acetylene side, Field and co-workers (*15*, *16*) have searched for spectroscopic signatures of vinylidene in highly vibrationally excited levels of HCCH, where the minimum energy isomerization path lies along the local-bending vibrational coordinates. Alternatively, the vinylidene well can be accessed directly by photodetachment of the vinylidene anion (H_2CC^-), and several research groups have used this approach to probe the spectroscopy and dynamics of neutral H_2CC (*17*-*21*).

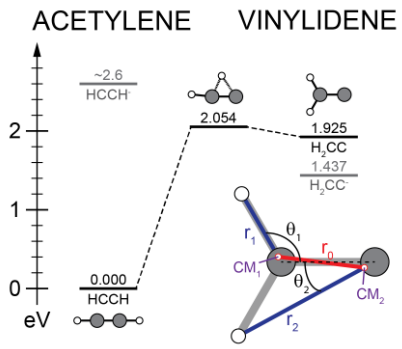

Figure 1. Energy diagram for the neutral vinylidene-acetylene isomerization. Energies (in eV, relative to HCCH) and geometries were obtained from Ref. (*21*). Experimental energies for the anions of both isomers are shown in gray; the H_2CC^- value was obtained from the present work, whereas the $HCCH^-$ value was estimated from electron scattering experiments (*28*). The CH—CH Jacobi coordinate system used to describe the isomerization is shown as an inset.

Previous photodetachment-based experiments have led to differing views regarding the timescale on which vinylidene isomerizes to acetylene. In an anion photoelectron spectroscopy study, Ervin *et al.* (*18*) observed that transitions to the $\tilde{X}^1A_1$ state of H_2CC were considerably broader than those arising from detachment to the higher-lying $\tilde{a}^3B_2$ state, for which the barrier to isomerization is significantly larger. The extra broadening of ground-state band features was attributed to isomerization on a sub-picosecond timescale. In contrast, later Coulomb explosion imaging (CEI) experiments by Vager (*19*) indicated that neutral H_2CC formed by anion photodetachment is stable on at least a microsecond timescale. It should be noted that lifetime is an ill-defined concept in such a system, as both acetylene and vinylidene are bound species whose eigenstates cannot form a true continuum. However, individual eigenstates may have varying degrees of mixing between zeroth-order states of the two isomers, especially near and above the isomerization barrier. This mixing has been explored in quantum dynamical simulations of the anion photoelectron spectrum starting with work by Bowman *(10)*, who found the simulated spectrum to be dominated by sharp peaks associated with isolated vinylidene eigenstates.

The aim of the current work was to experimentally characterize individual vibrational eigenstates of vinylidene and to understand the vibrational mode dependence of mixing with acetylene. To this end, we measured photodetachment spectra of H_2CC^- and D_2CC^- anions at higher resolution than previous work (*18*) using two complementary experimental methods, high-resolution photoelectron imaging (HR-PEI) (*22*) and slow electron velocity-map imaging of cryogenically-cooled anions (cryo-SEVI) (*23*). The experiments are supplemented by full-dimensional quantum dynamics calculations on a highly accurate *ab initio*-based potential

energy surface, carried out previously for the H_2CC-HCCH system (*12*, *24*) and expanded here by covering larger sections of configuration space in both isomeric regions.

The combination of experiment and theory shows that photodetachment directly accesses eigenstates that are mostly localized in the vinylidene well. The H_2CC and D_2CC isotopologues both undergo vibronic coupling to a high-lying vinylidene electronic state, which results in the appearance of nominally Franck-Condon (FC) forbidden transitions to neutral vibrational levels with excitation along non-totally-symmetric (b_2) modes. Most notable is the vibronic coupling-induced observation of features involving odd quanta of excitation in the in-plane rocking (ν_6) mode, which, for the H_2CC isotopologue, mixes strongly with the local-bending modes in the acetylene well. Isomerization is largely encoded in the spectra of vibrational states that involve excitation of this mode.

The experiments reported here used velocity-map imaging (VMI) detection schemes to measure the electron kinetic energy (eKE) distribution and photoelectron angular distribution (PAD) that result from electron photodetachment of mass-selected anions. The VMI spectrometer used in the HR-PEI measurements (fig. S1) was optimized to provide 0.7 to 25 cm^{-1} resolution over a wide range of eKE, so that a single photon energy (*hv*) could be used to obtain vibrationally-resolved spectra with reliable intensities and PADs. The cryo-SEVI spectrometer (fig. S2) provided higher resolution (sub-meV) over a narrower range of eKEs, assisted by cooling the anions to ~10 K prior to detachment to reduce spectral congestion arising from anion rotational and vibrational excitation. Together, the HR-PEI and cryo-SEVI techniques yield a more complete picture of the photoelectron eKE spectrum and PADs than when used separately.

The cryo-SEVI spectra of H_2CC^- and D_2CC^- (Fig. 2A) and the HR-PEI spectrum of H_2CC^- (Fig. 2B) display photoelectron intensity versus electron binding energy (eBE), where $\mathrm{eBE} = h\nu - \mathrm{eKE}$. All three spectra are dominated by the vibrational origin (A) and show transitions to vibrational levels up to ~4000 cm^{-1} above the vinylidene vibrational ground state.

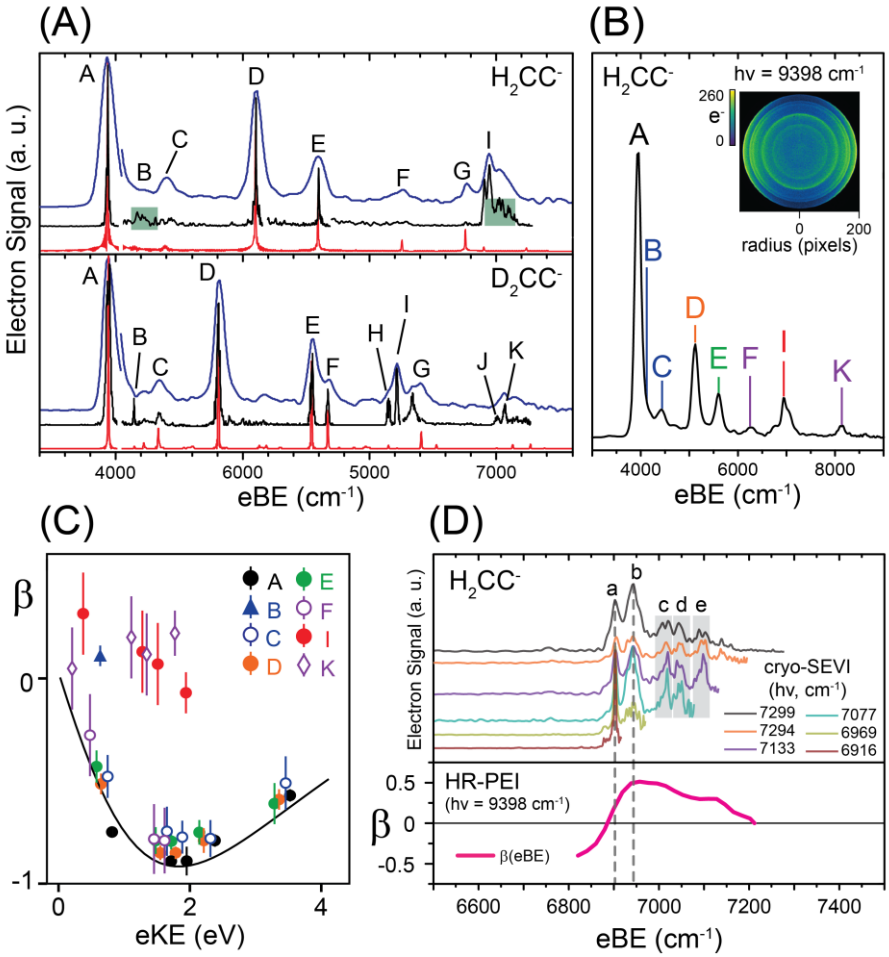

Figure 2. Vinylidene photoelectron spectra. A. Cryo-SEVI spectra of H_2CC^- (top) and D_2CC^- (bottom), as well as theoretical results for both isotopologues (red). The blue traces represent overview spectra while the black traces are higher resolution composite spectra; see section A of SM for more details. For clarity, all traces have been scaled by a factor of 2 following the break in the overview after peak A. **B.** HR-PEI spectrum of H_2CC^-. The image used to construct the spectrum is shown as an inset. **C.** PADs of various spectral features obtained from the HR-PEI H_2CC^- spectrum. The solid line shows a Hanstorp *p*-orbital detachment fit to the anisotropy parameter of peak A (*29*). Error bars correspond to one standard deviation of the anisotropy parameter obtained from the fitting process. **D.** Region I of the H_2CC^- photoelectron spectrum showing the underlying structure revealed by cryo-SEVI. The anisotropy parameter obtained from the HR-PEI spectrum is also shown to illustrate the variation in angular distribution across this region. Vertical dashed lines show how peaks a and b line up with the anisotropy parameter.

PADs are readily obtained from photoelectron images (SM section B), an example of which is shown in Fig. 2B. For each peak, the PADs yield the anisotropy parameter (β), which by definition falls between -1 and 2. These limits correspond to perpendicular and parallel detachment, respectively (*25*). Figure 2C shows β for several peaks as a function of eKE, obtained from HR-PEI measurements at several photon energies. The PADs extracted from the cryo-SEVI spectra (fig. S3) are in agreement with the HR-PEI results; with the exception of features B, I, and K, all peaks in the cryo-SEVI spectra of both isotopologues have $\beta < 0$ for eKEs below 1 eV, and peaks B, I, and K show distinctly positive β values at these kinetic energies.

The enhanced resolution of cryo-SEVI is evident in the considerably narrower linewidths in Fig. 2A compared to previous photoelectron spectra (*18*), and a direct comparison is shown in fig. S4. The linewidths of the vibrational origins and most of the other peaks are ~10 cm^{-1} and ~30 cm^{-1} in the H_2CC^- and D_2CC^- spectra, respectively, suggesting that these features are predominantly transitions that terminate in single eigenstates. These linewidths are primarily determined by the underlying rotational contours (fig. S5) and, as discussed previously (*21*) and in section C of SM, reflect the differing nuclear spin statistics for H and D atoms. In contrast to the previously published spectrum, the majority of features do not display significant broadening relative to the previously observed excited state features (*21*). However, there are several anomalously broadened and irregular regions (B, C and I) in the H_2CC^- cryo-SEVI spectrum, discussed in more detail below.

Comparison to the theoretical spectra in Fig. 2A (red traces) and figs. S6-7 allows unambiguous assignment of nearly all experimentally observed peaks, as shown in Table 1.

These assignments are particularly clear for D_2CC, where discrepancies between theory and experiment are <10 cm^{-1} for all features, excluding peak G. From the rotational contours of the 0_0^0 bands, we obtain electron affinities (EAs) of 0.4866(8) and 0.488(2) eV for H_2CC and D_2CC, respectively, as described in section C of the SM. These EAs lie within the error bars of the previously reported values (*18*) of 0.490(6) and 0.492(6) eV, respectively; they reflect our enhanced resolution and the ability to partially resolve the rotational structure of the band origins. Most of the remaining features in the two spectra can be attributed to FC-allowed transitions involving totally-symmetric (a_1) neutral vibrational levels, which, within the Born-Oppenheimer approximation, are the only transitions that can appear in the theoretical spectra for detachment from the anion vibrational ground state. Features B and I are nominally assigned to the FC-forbidden 6_0^1 and mixed 5_0^1 and $1_0^1 6_0^1$ transitions, both involving b_2-symmetric vibrational levels of neutral vinylidene.

These FC-forbidden transitions are attributed to Herzberg-Teller (HT) coupling to an excited electronic state with B_2 symmetry (SM sections B and C). The $\tilde{B}\,^1B_2$ state has been predicted to lie about 4 eV above the $\tilde{X}\,^1A_1$ state (*26*). We have observed detachment to this state (fig. S8), finding its term energy to be T_0 = 3.997(3) eV with respect to the $\tilde{X}\,^1A_1$ state and its anisotropy parameter to be positive. The derivative coupling between the $\tilde{X}\,^1A_1$ and $\tilde{B}\,^1B_2$ states has been calculated near the vinylidene minimum (section E in SM), and the interaction between these states is found to be localized largely along the ν_6 mode, with a minor contribution from the ν_5 mode. Peaks B and I also exhibit positive anisotropy parameters (Fig. 2C), in contrast to all of the FC-allowed features, consistent with HT coupling between the two electronic states (*27*). Moreover, as discussed in section C of SM, the rotational selection rules

for photodetachment differ for the FC-allowed ($\Delta K_a = \pm 1$) vs. HT-allowed ($\Delta K_a = 0$) transitions, leading to the narrower rotational profiles of peaks B and I (7 and 16 cm^{-1} fwhm, respectively) in the D_2CC^- SEVI spectrum relative to the FC-allowed transitions.

Overall, the D_2CC^- cryo-SEVI spectrum is what would be expected for a well-behaved, stable molecule, albeit one that exhibits HT coupling with an excited electronic state. The same is true for much of the H_2CC^- spectrum, with the exception of features B, C, and I. Features B and C, assigned to the 6_0^1 and 6_0^2 transitions, appear in the cryo-SEVI spectrum as broad, weak features, even at high resolution (black trace, Figure 2A). The spectral broadening indicates participation of multiple eigenstates, each of which carries some vinylidene oscillator strength. Figure 2D shows that feature I, in the vicinity of the calculated 5_0^1 and $1_0^1 6_0^1$ transitions, resolves

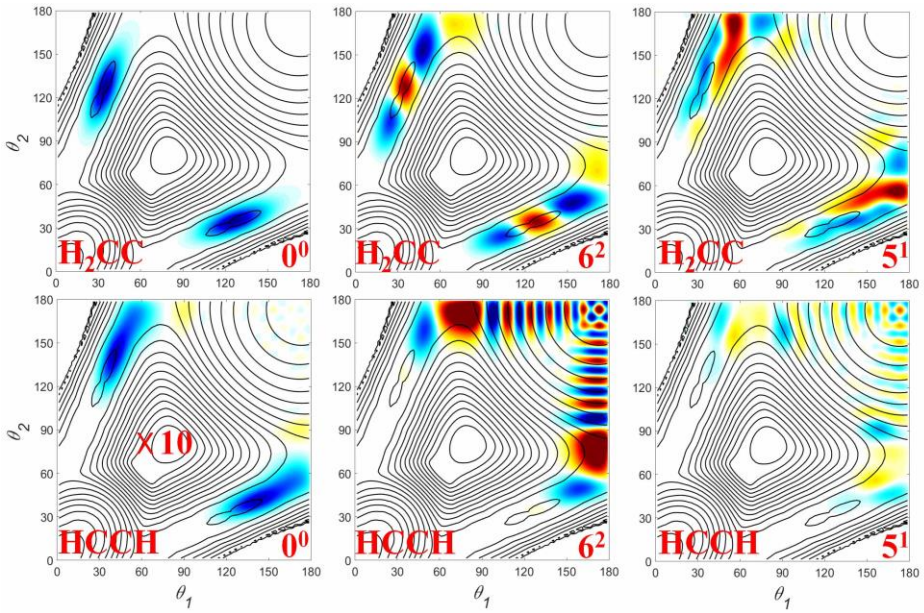

Figure 3. Calculated wavefunctions for neutral vibrational levels of H_2CC. Wavefunctions of the 0^0, 6^2, and 5^1 states are shown along the θ_1 and θ_2 directions of the CH—CH Jacobi coordinates, with the coordinate r_0 taking the equilibrium value of H_2CC (top) or HCCH (bottom) and the wavefunctions summed over the remaining coordinates. The acetylene component is dominated by local-bender states along the θ_1, $\theta_2 \sim 180^o$ axes. The two-dimensional potential energy surface is superimposed, in which the $\theta_1 = \theta_2 = 180^o$ well corresponds to HCCH.

into a cluster of five closely-spaced, narrow peaks (a-e, energies in table S1). Comparison with the HR-PEI angular distribution reveals notable variation in the anisotropy parameter across this series of peaks, with a considerably lower β value for peak 'a' than peaks 'b-e'. In addition, the intensity of peak 'a' decreases more slowly than the other features as the photon energy is lowered. Both observations indicate variation of the partial wave contributions to photodetachment across region I, suggesting that the electronic characters of the final eigenstates are highly variable.

To understand how the isomerization mechanism is encoded in the neutral eigenstates, and to gain additional insights into the experimental spectra, we turn to the calculated wavefunctions for the lowest two FC-allowed vibrational eigenstates populated by photodetachment of H_2CC^- anions (0^0 and 6^2) and a state allowed only by HT coupling (5^1). Using the CH—CH Jacobi coordinates shown in the inset of Fig. 1, the wavefunctions are plotted in Fig. 3, superimposed on a contour plot of the potential energy surface. In the top and bottom panels, the distance between CH centers-of-mass (r_0) is constrained to either the vinylidene or acetylene equilibrium value, respectively, so that the bending wavefunctions are shown for both the vinylidene and acetylene wells. For the ground vinylidene state (0^0), there is very little acetylene character, indicating strong localization in the vinylidene well. However, excitation of the in-plane rocking mode of vinylidene (6^2) introduces appreciable acetylene character, featuring highly excited states in the local-bending coordinates (local-benders), evidenced by the large number of nodes along the angular coordinates (θ_1, θ_2) (*15*).

The plots in Fig. 3 and S9 also show that the neutral 5^1 state mixes with the $1^1 6^1$ state through an anharmonic interaction, giving region I its intensity through the ν_6-dominated HT

coupling. This interaction is enhanced by the energy-lowering of the $1^1 6^1$ state relative to the sum of the ν_1 and ν_6 fundamentals, due to the strong inter-mode anharmonicity between the stretching and rocking modes. The other peaks in Feature I could be due to higher b_2 states such as $5^1 6^2$ and other nearby FC-allowed transitions.

Fig. 3 shows that this mixed $5^1 \sim 1^1 6^1$ state exhibits appreciable acetylene character along the local-bending coordinates, with similar nodal structure as is seen for the 6^2 state. This result links the spectroscopy of vinylidene to its isomerization dynamics; the minimum energy isomerization pathway follows the rocking normal mode of vinylidene, which ultimately connects with the local-bending vibrational states of acetylene. Indeed, the acetylenic contributions to the 6^2 and $5^1 \sim 1^1 6^1$ eigenfunctions involve strong admixtures of the local-bending excitation, which has been extensively probed by spectroscopic studies of highly excited acetylene (*15*). For D_2CC, the extent of mixing with DCCD is negligible, presumably owing to the much narrower eigenfunctions resulting in suppressed tunneling. The wavefunctions for other H_2CC and D_2CC states can be found in figs. S9-11.

Chemically, isomerization entails the breaking and formation of bonds within a molecule. To understand the dynamics of the 1,2-hydrogen shift in this system, one needs to quantum mechanically simulate transitions between various vibrational eigenstates that have different amplitudes of the zeroth-order vinylidene (^{1}) and acetylene (^{2}) basis states: $\Psi_n^{(neutral)} \approx c_n^{(1)} \psi_n^{(1)} + c_{nm}^{(2)} \psi_m^{(2)}$. The extent of mixing, which encodes the isomerization, depends on the energy difference between $\psi_n^{(1)}$ and $\psi_m^{(2)}$ as well as the strength of the interaction matrix element between the two. As mentioned above, the acetylene states involved in the mixing

($\psi_m^{(2)}$) are mostly the local-benders, which have a much smaller density of states than the total density of acetylene vibrational states. The spectral intensity of a peak in the photoelectron spectrum is primarily determined by $I_n \approx \left|c_n^{(1)}\right|^2 \left|\left\langle \psi_n^{(1)} \middle| \Psi^{(anion)} \right\rangle\right|^2$. The vinylidene weights, $\left|c_n^{(1)}\right|^2$, can be approximately extracted from the calculated H_2CC and D_2CC eigenfunctions and are listed in Table 1. For H_2CC, only those final states with ν_6 excitation mix strongly with HCCH, whereas for D_2CC, the mixing with DCCD is much smaller due to the narrower wavefunctions.

The cryo-SEVI and HR-PEI spectra, with the supporting theoretical analysis, offer insights into the vinylidene-acetylene isomerization and its influence on the vinylidene photoelectron spectrum. Most neutral vibrational states formed via photodetachment are dominated by vinylidene character for both isotopologues, an observation consistent with the main conclusion of the CEI experiment (*19*) and the calculations by Bowman (*10*). However, H_2CC states in which the ν_6 mode is excited show non-negligible acetylene character, which manifests as spectral broadening and/or fine structure for this isotopologue. Excitation of this mode can occur through FC-allowed transitions (6^2), vibronic coupling via an excited state of vinylidene (6^1), or anharmonic coupling between ground state vibrational levels ($5^1 \sim 1^1 6^1$). This spectroscopic result implies that in the range of excitation energies probed here, the isomerization of vinylidene to acetylene is highly state-specific and is promoted by excitation of the ν_6 mode. Significantly less coupling to acetylene is observed for D_2CC, which suggests that isomerization of D_2CC is considerably less facile even when the ν_6 mode is excited. These insights provide a quantum mechanical foundation for understanding the 1,2-hydrogen shift reaction.

References:

1. Y. Yamamoto, S. I. Murahashi, I. Moritani, Direct and sensitized photodecompositions of 1-phenyldiazoethane: the spin state in the 1,2-hydrogen migration to the carbene center. *Tetrahedron* **31**, 2663-2667 (1975).
2. P. J. Stang, Unsaturated carbenes. *Chem. Rev.* **78**, 383 (1978).
3. P. S. Skell, J. E. Villaume, F. A. Fagone, Formation of vinylidene intermediates in the reaction of diatomic carbon with propylene. *J. Am. Chem. Soc.* **94**, 7866 (1972).
4. A. H. Laufer, An excited state of acetylene: photochemical and spectroscopic evidence. *J. Chem. Phys.* **73**, 49-52 (1980).
5. M. M. Hills, J. E. Parmeter, W. H. Weinberg, Chemisorption and reaction of ethylene on chemically modified Ru(001) surfaces. *J. Am. Chem. Soc.* **109**, 4224 (1987).
6. M. Ahmed, D. S. Peterka, A. G. Suits, The photodissociation of the vinyl radical (C_2H_3) at 243 nm studied by velocity map imaging. *J. Chem. Phys.* **110**, 4248 (1999).
7. J. Zador, M. D. Fellows, J. A. Miller, Initiation reactions in acetylene pyrolysis. *J. Phys. Chem. A* **121**, 4203-4217 (2017).
8. T. Carrington, L. M. Hubbard, H. F. Schaefer, W. H. Miller, Vinylidene: potential energy surface and unimolecular reaction dynamics. *J. Chem. Phys.* **80**, 4347-4354 (1984).
9. R. L. Hayes, E. Fattal, N. Govind, E. A. Carter, Long live vinylidene! A new view of the $H_2CC \rightarrow HCCH$ rearrangement from ab initio molecular dynamics. *J. Am. Chem. Soc.* **123**, 641 (2001).
10. S. Zou, J. M. Bowman, A. Brown, Full-dimensionality quantum calculations of acetylene-vinylidene isomerization. *J. Chem. Phys.* **118**, 10012 (2003).
11. H. Lee, J. H. Baraban, R. W. Field, J. F. Stanton, High-accuracy estimates for the vinylidene-acetylene isomerization energy and the ground state rotational constants of $:C=CH_2$. *J. Phys. Chem. A* **117**, 11679 (2013).
12. H. Han, A. Li, H. Guo, Toward spectroscopically accurate global ab initio potential energy surface for the acetylene-vinylidene isomerization. *J. Chem. Phys.* **141**, 244312 (2014).
13. Y. Ren, W. Bian, Mode-specific tunneling splittings for a sequential double-hydrogen transfer case: an accurate quantum mechanical scheme. *J. Phys. Chem. Lett.* **6**, 1824-1829 (2015).

14. J. K. Lundberg, R. W. Field, C. D. Sherrill, E. T. Seidl, Y. Xie, H. F. Schaefer, Acetylene: Synergy between theory and experiment. *J. Chem. Phys.* **98**, 8384-8391 (1993).

15. M. P. Jacobson, R. W. Field, Acetylene at the threshold of isomerization. *J. Phys. Chem. A* **104**, 3073-3086 (2000).

16. M. P. Jacobson, J. P. O'Brien, R. W. Field, Anomalously slow intramolecular vibrational redistribution in the acetylene $X\ ^1\Sigma_g^+$ state above 10000 cm^{-1} of internal energy. *J. Chem. Phys.* **109**, 3831 (1998).

17. S. M. Burnett, A. E. Stevens, C. S. Feigerle, W. C. Lineberger, Observation of X^1A_1 vinylidene by photoelectron spectroscopy of the vinylidene ($C_2H_2^-$) ion. *Chem. Phys. Lett.* **100**, 124-128 (1983).

18. K. M. Ervin, J. Ho, W. C. Lineberger, A study of the singlet and triplet states of vinylidene by photoelectron spectroscopy of $H_2C{=}C^-$, $D_2C{=}C^-$, and $HDC{=}C^-$. Vinylidene-acetylene isomerization. *J. Chem. Phys.* **91**, 5974-5992 (1989).

19. J. Levin, H. Felman, A. Baer, D. Ben-Hamu, O. Heber, D. Zajfman, Z. Vager, Study of unimolecular reactions by Coulomb explosion imaging: the nondecaying vinylidene. *Phys. Rev. Lett.* **81**, 3347 (1998).

20. H. K. Gerardi, K. J. Breen, T. L. Guasco, G. H. Weddle, G. H. Gardenier, J. E. Laaser, M. A. Johnson, Survey of Ar-tagged predissociation and vibrationally mediated photodetachment spectroscopies of the vinylidene anion, $C_2H_2^-$. *J. Phys. Chem. A* **114**, 1592-1601 (2010).

21. J. A. DeVine, M. L. Weichman, X. Zhou, J. Ma, B. Jiang, H. Guo, D. M. Neumark, Non-adiabatic effects on excited states of vinylidene observed with slow photoelectron velocity-map imaging. *J. Am. Chem. Soc.* **138**, 16417-16425 (2016).

22. S. J. Cavanagh, S. T. Gibson, M. N. Gale, C. J. Dedman, E. H. Roberts, B. R. Lewis, High-resolution velocity-map-imaging photoelectron spectroscopy of the O^- photodetachment fine-structure transitions. *Phys. Rev. A* **76**, 052708 (2007).

23. C. Hock, J. B. Kim, M. L. Weichman, T. I. Yacovitch, D. M. Neumark, Slow photoelectron velocity-map imaging spectroscopy of cold negative ions. *J. Chem. Phys.* **137**, 244201 (2012).

24. L. Guo, H. Han, J. Ma, H. Guo, Quantum dynamics of vinylidene photodetachment on an accurate global acetylene-vinylidene potential energy surface. *J. Phys. Chem. A* **119**, 8488-8496 (2015).

25. J. Cooper, R. N. Zare, Angular distribution of photoelectrons. *J. Chem. Phys.* **48**, 942 (1968).

26. S. Boyé-Péronne, D. Gauyacq, J. Liévin, Theoretical description of electronically excited vinylidene up to 10 eV: First high level ab initio study of singlet valence and Rydberg states. *J. Chem. Phys.* **141**, 174317 (2014).

27. K. M. Ervin, W. C. Lineberger, Photoelectron-spectra of C_2^- and C_2H. *J. Phys. Chem.* **95**, 1167-1177 (1991).

28. R. Dressler, M. Allan, A dissociative electron-attachment, electron transmission, and electron energy-loss study of the temporary negative-ion of acetylene. *J. Chem. Phys.* **87**, 4510-4518 (1987).

29. D. Hanstorp, C. Bengtsson, D. J. Larson, Angular distributions in photodetachment from O^-. *Phys. Rev. A* **40**, 670-675 (1989).

30. C. J. Dedman, E. H. Roberts, S. T. Gibson, B. R. Lewis, Fast 1kV MOSFET switch. *Rev. Sci. Instrum.* **72**, 3718-3720 (2001).

31. A. T. J. B. Eppink, D. H. Parker, Velocity map imaging of ions and electrons using electrostatic lenses: Application in photoelectron and photofragment ion imaging of molecular oxygen. *Rev. Sci. Instrum.* **68**, 3477 (1997).

32. J. R. Gascooke, S. T. Gibson, W. D. Lawrance, S. T. Gibson, A "circularisation" method to repair deformations in velocity map images. *J. Chem. Phys.* **147**, 013924 (2017).

33. D. D. Hickstein, R. Yurchak, D. Das, C.-Y. Shih, *PyAbel (v0.7): A Python package for Abel transforms*, https://github.com/PyAbel/PyAbel (2016).

34. E. W. Hansen, P.-L. Law, Recursive methods for computing the Abel transform and its inverse. *J. Opt. Soc. Am.* **2**, 510-520 (1985).

35. A. Osterwalder, M. J. Nee, J. Zhou, D. M. Neumark, High resolution photodetachment spectroscopy of negative ions via slow photoelectron imaging. *J. Chem. Phys.* **121**, 6317 (2004).

36. D. M. Neumark, Slow electron velocity-map imaging of negative ions: applications to spectroscopy and dynamics. *J. Phys. Chem. A* **112**, 13287 (2008).

37. U. Even, J. Jortner, D. Noy, N. Lavie, C. Cossart-Magos, Cooling of large molecules below 1K and He clusters formation. *J. Chem. Phys.* **112**, 8068-8071 (2000).

38. J. H. J. Dawson, K. R. Jennings, Production of gas-phase radical-anions by reaction of O^- ions with organic substrates. *J. Chem. Soc., Faraday Trans. 2* **72**, 700-706 (1976).

39. W. C. Wiley, I. H. McLaren, Time-of-flight mass spectrometer with improved resolution. *Rev. Sci. Instrum.* **26**, 1150-1157 (1955).

40. A. M. Oliveira, Y. J. Lu, J. H. Lehman, P. B. Changala, J. H. Baraban, J. F. Stanton, W. C. Lineberger, Photoelectron spectroscopy of the methide anion: electron affinities of CH_3 and CD_3 and inversion splittings of CH_3^- and CD_3^-. *J. Am. Chem. Soc.* **137**, 12939-12945 (2015).

41. D. W. Chandler, P. L. Houston, Two-dimensional imaging of state-selected photodissociation products detected by multiphoton ionization. *J. Chem. Phys.* **87**, 1445-1447 (1987).

42. M. L. Weichman, J. A. DeVine, D. S. Levine, J. B. Kim, D. M. Neumark, Isomer-specific vibronic structure of the 9-, 1-, and 2-anthracenyl radicals via slow photoelectron velocity-map imaging. *Proc. Natl. Acad. Sci. USA* **113**, 1698-1705 (2016).

43. B. Dick, Inverting ion images without Abel inversion: maximum entropy reconstruction of velocity maps. *Phys. Chem. Chem. Phys.* **16**, 570-580 (2014).

44. C. Blondel, W. Chaibi, C. Delsart, C. Drag, F. Goldfarb, S. Kröger, The electron affinities of O, Si, and S revisited with the photodetachment microscope. *Eur. Phys. J. D* **33**, 335-342 (2005).

45. U. Berzinsh, M. Gustafsson, D. Hanstorp, A. Klinkmuller, U. Ljungblad, A. M. Martenssonpendrill, Isotope shift in the electron-affinity of chlorine. *Phys. Rev. A* **51**, 231 (1995).

46. K. J. Reed, A. H. Zimmerman, H. C. Andersen, J. I. Brauman, Cross sections for photodetachment of electrons from negative ions near threshold. *J. Chem. Phys.* **64**, 1368 (1976).

47. G. Herzberg, *Electronic Spectra of Polyatomic Molecules*. Molecular Spectra and Molecular Structure (D. Van Nostrand Company, Inc., Princeton, NJ, 1945), vol. 3.

48. A. Sanov, Laboratory-frame photoelectron angular distributions in anion photodetachment: insight into electronic structure and intermolecular interactions. *Annu. Rev. Phys. Chem.* **65**, 341 (2014).

49. R. Signorell, F. Merkt, General symmetry selection rules for the photoionization of polyatomic molecules. *Mol. Phys.* **92**, 793-804 (1997).

50. P. R. Bunker, P. Jensen, in *Molecular Symmetry and Spectroscopy*, R. H. Haynes, Ed. (National Research Council of Canada, Ottawa, Ontario, Canada, 1998).

51. C. M. Western, PGOPHER: A program for simulating rotational, vibrational, and electronic spectra. *J. Quant. Spectrosc. Rad.* **186**, 221 (2017).

52. R. Wester, Radiofrequency multipole traps: tools for spectroscopy and dynamics of cold molecular anions. *J. Phys. B: At. Mol. Opt. Phys.* **42**, 153001 (2009).

53. J. C. Light, T. Carrington Jr., Discrete-variable representations and their utilization. *Adv. Chem. Phys.* **114**, 263-310 (2000).

54. R. Chen, H. Guo, The Chebyshev propagator for quantum systems. *Comput. Phys. Commun.* **119**, 19-31 (1999).

55. R. Chen, G. Ma, H. Guo, Six-dimensional quantum calculation of highly excited vibrational energy levels of hydrogen peroxide and its deuterated isotopomers. *J. Chem. Phys.* **114**, 4763-4774 (2001).

56. H. Guo, Recursive solutions to large eigenproblems in molecular spectroscopy and reaction dynamics. *Rev. Comput. Chem.* **25**, 285-347 (2007).

57. M. P. Jacobson, C. Jung, H. S. Taylor, R. W. Field, State-by-state assignment of the bending spectrum of acetylene at 15000 cm^{-1}: a case study of quantum-classical correspondence. *J. Chem. Phys.* **111**, 600-618 (1999).

58. D. Xu, R. Chen, H. Guo, Probing highly excited vibrational eigenfunctions using a modified single Lanczos method: Application to acetylene (HCCH). *J. Chem. Phys.* **118**, 7273-7282 (2003).

59. H. Lischka, T. Muller, P. G. Szalay, I. Shavitt, R. M. Pitzer, R. Shepard, COLUMBUS-a program system for advanced multireference theory calculations. *Wires Comput. Mol. Sci.* **1**, 191-199 (2011).

60. B. H. Lengsfield, D. R. Yarkony, in *Advances in Chemical Physics: State-Selected and State-To-State Ion-Molecule Reaction Dynamics, Part 2, Theory,* M. Baer. and C.-Y. Ng, Ed. (John Wiley & Sons, Inc., 1992), vol. 82.

61. H. Lischka, M. Dallos, P. G. Szalay, D. R. Yarkony, R. Shepard, Analytic evaluation of nonadiabatic coupling terms at the MR-CI level. I. Formalism. *J. Chem. Phys.* **120**, 7322 (2004).

62. H. Lischka, M. Dallos, P. G. Szalay, D. R. Yarkony, R. Shepard, Analytic evaluation of nonadiabatic coupling terms at the MR-CI level. II. Minima on the crossing seam: Formaldehyde and the photodimerization of ethylene. *J. Chem. Phys.* **120**, 7330 (2004).

Acknowledgments: The experimental part of this research was funded by the Air Force Office of Scientific Research (No. FA9550-16-1-0097 to D.M.N.) and the Australian Research Council Discovery Project (No. DP160102585 to S.T.G.). M.L.W. thanks the National Science Foundation for a graduate research fellowship. Experimental data are available upon request from dneumark@berkeley.edu (cryo-SEVI) and stephen.gibson@anu.edu.au (HR-PEI). Theoretical work was funded by the National Natural Science Foundation of China (No. 91441107 to J.M.), the Air Force Office of Scientific Research (No. FA9550-15-1-0305 to H.G.), and the National Science Foundation (No. CHE-1361121 to D.R.Y.). R.W.F. gratefully acknowledges the Department of Energy, Office of Science, Chemical Sciences Geosciences and Biosciences Division of the Basic Energy Sciences Office (No. DE-FG0287ER13671).

Table 1. Peak positions (cm^{-1}), experimental and theoretical shifts from the vibrational origin (cm^{-1}), and assignments for the H_2CC^- and D_2CC^- ground state photoelectron spectra. Shifts were extracted from the cryo-SEVI scans, and HR-PEI peak positions for H_2CC^- are shown for comparison. Cryo-SEVI peak positions were extracted from the high-resolution (black) traces in Figure 2A unless otherwise noted. Uncertainties in peak positions correspond to one-σ, obtained from a Gaussian fit to the experimental trace.

	H_2CC^-					D_2CC^-				Assignment
Peak	HR-PEI eBE	eBE	Shift	Theo.	H_2CC%	eBE	Shift	Theo.	D_2CC%	
A	3940(60)	3935(7)	0	0.0	100	3941(17)	0	0.0	100	0_0^0
B	--	4190(50)*	255	283.2	84	4143(3)	202	203.9	100	6_0^1
C	4400(90)	4402(52)†	470	454.1	58	4345(18)	404	396.8	98	6_0^2
D	5120(60)	5103(5)	1168	1166.0	97	4809(11)	868	868.6	100	3_0^1
E	5570(50)	5597(4)	1662	1659.6	97	5547(10)	1606	1601.8	99	2_0^1
F	6250(80)	6240(70)†	2305	2322.6	96	5671(8)	1730	1730.0		3_0^2
G	6740(70)	6780(60)†	2845	2822.0	97	6339(18)	2398	2468.0		$2_0^1 3_0^1$
H				2967.7		6152(12)	2211	2206.7		1_0^1
I	6950(50)	6943(12)‡	3008	3013.7	82	6216(7)	2275	2276.9	99	5_0^1
				3117.6	68			2389.9	95	$1_0^1 6_0^1$
J						7008(14)	3067	3059.7		$1_0^1 3_0^1$
K	8130(70)	8125(41)†	4190	4218.4		7065(12)	3124	3125.5		$3_0^1 5_0^1$

*Peak position obtained by fitting the highlighted region B in Figure 2A to a single Gaussian.

† These features did not maintain sufficient intensity near-threshold to appear in high-resolution cryo-SEVI scans, and thus the eBEs are obtained from the lower-resolution overview scans (blue traces) in Figure 2A.

‡ Reported position corresponds to feature b in Fig. 2D.

Supplementary Materials:

Materials and Methods
Supplementary Text
Figures S1 to S12
Tables S1 to S3
References (*30-62*)

Supplementary Materials:

A. Experimental methods

a. High-resolution photoelectron imaging (HR-PEI)

A schematic of the HR-PEI setup is shown in Figure S1, with the major components labeled. Further details of the apparatus are given in Ref. (*22*). Vinylidene anions are produced by passing pure ethylene gas through a pulsed valve, which then undergoes supersonic expansion into a high-voltage discharge. Negative ions are extracted, accelerated to 500 eV, and focused into an ion gating, bunching, and potential re-referencing unit (*30*). The ions are separated by *m*/*z* over a 2m time-of-flight (TOF) region, and an electrostatic gate selects the mass packet of interest. This ion packet is directed to the interaction region of a VMI electrostatic lens, where it is crossed with a detachment laser beam.

Several laser configurations were used to obtain the HR-PEI data presented in this work, employing a Continuum Powerlite 9010 Nd:YAG laser either alone or as a pump for a Sunlite EX optical parametric oscillator (OPO). The photoelectron spectrum in Figure 2B was measured using the fundamental output of the Nd:YAG laser (1064nm). The anisotropy parameters in Figure 2C were determined using a number of photon energies; energies of 20247, 17271, 16155, 15649, and 15244 cm^{-1} were obtained by using the third harmonic (355nm) of the Nd:YAG laser to pump the OPO, and additional data points were obtained by directly using the third harmonic and fundamental output of the Nd:YAG laser (28169 and 9398 cm^{-1}, respectively).

The VMI lens is a modified version of the original concept of Eppink and Parker (*31*). Photodetached electrons are velocity-mapped to a 75mm diameter microchannel plate/phosphor screen detector (Burle). The MCP screen is gated to ensure that unwanted events from untargeted ions and neutral species are not detected. Images from the phosphor are captured by a 2048×2048 pixel monochrome CCD camera (PCO 2000), and each camera frame is transferred to a computer at the 10 Hz laser repetition rate. Camera frames are processed in real time to identify events, which are centroided and binned into a rectangular pixel-grid image. This image may be of arbitrary pixel number, with a larger image pixel number providing finer detail at the expense of greater statistical uncertainty in the individual pixel intensities. The accumulated image is circularized by an angular-dependent radial scaling determined through a comparison of adjacent radial intensity profiles (*32, 33*). In this work, the radial correction to reduce image distortion is applied to the raw (*x,y*)-centroid data prior to forming the velocity-map image, eliminating any requirement for image pixel intensity interpolation.

The photoelectron velocity distribution is obtained from the velocity-mapped image by an inverse Abel transformation, which is based on the algorithm of Hansen and Law (*34*) and described in more detail on the *PyAbel* website (*33*). For the low-distortion HR-PEI images, all quadrants are equivalent and may be combined to improve the statistical accuracy of the inverse Abel transform and, hence, the photoelectron spectrum and photoelectron angular distributions. Energy calibration is obtained using a single scaling factor (i.e., $eKE = a\ R^2$, where R is the radius in pixels), to align the origin peak with the known electron affinity of vinylidene (*18*).

The relative kinetic energy resolution is approximately constant for VMI experiments. The HR-PEI spectrometer achieves sub-cm^{-1} resolution for slow electrons detached from atomic species. In this study, a more quantitative comparison comes from a parallel measurement of the photoelectron spectrum of O_2^-, which has a similar electron affinity (3613 cm^{-1}) to vinylidene. A rotational model band decomposition gives a rotational linewidth of 10.1(1) cm^{-1} for the $v' = 2$ transition, for detachment at 9398 cm^{-1}.

The experimental anisotropy parameters in Figure 2C are obtained by fitting Eq. (0), explained in more detail in Section B, to radially-integrated transition intensities. For a single quadrant of a given image, the intensity variation is linear in $P_2(\cos\theta)$, with slope equal to $\beta \times$ intercept. The most accurate anisotropy parameter determinations occur for the stronger transitions.

b. Cryo-SEVI

The cryo-SEVI method has been described previously in detail (*23, 35, 36*), and a layout of the machine is shown in Figure S2A. As described in the cryo-SEVI study of electronically excited vinylidene (*21*), anions are formed by supersonic expansion of a precursor gas mix (trace N_2O, C_2H_4 or C_2D_4, and He) through an Even-Lavie valve (*37*) equipped with a pulsed filament ionizer. Injection of electrons from the ionizer results in dissociative electron attachment to N_2O, forming O^- which proceeds to react with C_2H_4 (99.5%, Praxair) or C_2D_4 (99%, Sigma Aldrich) to form H_2CC^- or D_2CC^- (*38*). The ions are guided through a radiofrequency (rf) hexapole ion guide and rf quadrupole mass filter and then deposited into a rf octupole ion trap held at 5 K and filled with a buffer gas mixture of 20% H_2 in He (*23*). Ions are stored in the trap for ~40 ms, during which they undergo collisions with the buffer gas resulting in thermalization with the cryogenically-cooled trap. Ions are then extracted into an orthogonal Wiley-McLaren time-of-flight mass spectrometer (*39*) and focused into the interaction region of a VMI spectrometer (*31*), where they are photodetached by a tunable laser.

In this work, several different laser schemes have been used for photodetachment. The overview spectra in Figure 2A (blue traces) were obtained using the fundamental output of an Nd:YAG laser (1064 nm, 9398 cm^{-1}). The higher-resolution scans (black traces) were taken using a home-built IR difference frequency generation (IR-DFG) setup covering the mid-IR (1.3-4 μm, 2500-7692 cm^{-1}), which is similar in design to the setup described by Lineberger and co-workers (*39*). Further details of the IR-DFG setup are reported below. The IR laser wavelengths for the high resolution traces were chosen in order to maximize direct detachment; there are narrow vibrational anion resonances in the vicinity of the origin band that undergo autodetachment (*20*), leading to photoelectron spectra that vary strongly with photon energy. The photon energies used in Figure 2A do not access these resonances. To observe detachment to the $\tilde{B}^1B_2$ electronic state, the third harmonic of an Nd:YAG laser (355 nm, 28169 cm^{-1}) was used to pump the tunable dye laser, the output of which was then frequency-doubled yielding tunable UV light (255-280 nm, 35714-39216 cm^{-1}).

Following photodetachment, the VMI lens projects and focuses the detached electron Newton spheres onto a 2D detector comprising two chevron-stacked microchannel plates coupled to a phosphor screen. The back of the phosphor screen is photographed by a CCD camera with each laser shot (*41*). Each photograph is analyzed for single electron events, the

centroids of which are calculated and binned in a grid sufficiently fine to ensure that resolution is not limited by pixel size (*42*). The radial and angular photoelectron velocity distributions are reconstructed from the accumulated images using the Maximum Entropy Velocity Legendre Reconstruction (MEVELER) method (*43*). The photoelectron spectrum (in eKE) is obtained from the resultant radial distribution, and subsequently converted to eBE by energy conservation (eBE = $h\nu$ – eKE); photoelectron angular distributions will be discussed in Section B of this document, and are shown for several features in the cryo-SEVI spectra of both isotopologues in Figure S3.

The spectrometer is calibrated using SEVI images of the well-characterized photodetachment transitions of atomic anions. For the ground state electronic band, images of O^- (*44*) were obtained using the tunable red dye laser light aligned through the machine to be perfectly collinear with the DFG light. For detachment to the $\tilde{B}^1B_2$ excited state, Cl^- was used as a calibrant (*45*). Figure S4 shows a direct comparison between the cryo-SEVI H_2CC^- spectrum and the spectrum reported by Lineberger and co-workers (*18*), showing the good agreement and improved resolution in the current results.

i. Infrared difference frequency generation (IR-DFG)

The IR-DFG setup is shown schematically in Figure S2B. A dye laser pumped by the 532 nm second harmonic of a pulsed, injection-seeded Nd:YAG laser produces red light (590-840 nm). This is mixed with residual 1064 nm Nd:YAG fundamental light in a non-linear $LiNbO_3$ DFG crystal, producing mid-IR light with a frequency corresponding to the difference between the Nd:YAG fundamental and dye laser frequency. Tunability is achieved by varying the wavelength of the dye laser output.

The $LiNbO_3$ DFG crystal used in this work is 16×11×30 mm in size, is cut at 56º (Sirah Lasertechnik, DFM-2400-T), and can produce 1.3-2.5 μm DFG light using 590-750 nm dye laser light. The crystal is placed in a motorized rotating mount with its optical axis parallel to the laser table. As this crystal is designed for a type-I nonlinear process, the red dye laser light must be polarized horizontally (extraordinary to the crystal optical axis) while the 1064 nm and DFG light must be polarized vertically (ordinary to the crystal optical axis). As it was found that the 1064 nm light leaves the Nd:YAG laser with poorly defined elliptical polarization, a combination of two thin film polarizers and one half-wave plate is used to prepare a vertically polarized 1064 nm beam with tunable power. As the dye laser output is vertically polarized, an achromatic half-wave plate is used to prepare horizontally polarized red light.

DFG output at a given wavelength is optimized by slowly rotating the $LiNbO_3$ DFG crystal angle while monitoring the IR intensity on a sensitive pyroelectric detector. A $LiNbO_3$ compensating crystal rotates in an opposite direction to the DFG crystal, so the beam path is unchanged for phase matching conditions at different wavelengths.

All optics downstream of the DFG crystal are made of CaF_2 or MgF_2 to minimize absorption of mid-IR light. CaF_2 mirrors coated for 1064 nm and 600-900 nm light dump the initial wavelengths and transmit the DFG light. The DFG light is aligned through the SEVI machine using CaF_2 prisms, and is focused into the interaction region using a cylindrical CaF_2 lens with a 0.5 m focal length. The vacuum chamber windows are MgF_2.

B. Photoelectron angular distributions and vibronic coupling

The photoelectron angular distribution (PAD) associated with each photodetachment feature can be extracted from a given VMI image, and is given by (*25*)

$$\frac{d\sigma}{d\Omega} = \frac{\sigma_{tot}}{4\pi}\left[1 + \beta P_2(\cos\theta)\right]. \quad (0)$$

Here, σ_{tot} is the total detachment cross section for the transition in question, $P_2(x)$ is the second-order Legendre polynomial, θ is the angle of the photoelectron's velocity vector with respect to the laser polarization axis, and β is the anisotropy parameter, ranging from -1 (perpendicular detachment) to +2 (parallel detachment). The value of β is directly related to the angular momentum of the outgoing photoelectron and thus reflects the electronic character of the detached anion molecular orbital (*22, 29, 46*).

The MEVELER method used to reconstruct cryo-SEVI images (*43*) provides as output the projections of the reconstructed velocity-map image onto the zeroth and second-order Legendre polynomials as a function of radial distance, or equivalently, eKE. The zeroth-order projection (Q_0) contains the photoelectron spectrum, whereas the second-order projection (Q_2) contains the angular information. Given these, the anisotropy parameter β is given by

$$\beta = \frac{\int_{R_1}^{R_2} Q_2(R)dR}{\int_{R_1}^{R_2} Q_0(R)dR} \quad (0)$$

where R_1 and R_2 are limits set so that the integration is carried out over the peak of interest. Calculated β values at several detachment energies for key features in the cryo-SEVI spectra of both isotopologues are presented in Figure S3. Alternatively, a plot of β versus eBE for a single photon energy, such as that shown in Figure 2D, can be constructed by performing the integration on an interpolation of the (discrete) MEVELER output, with the limits of integration defined by the spacing between data points.

As can be seen in Figures 2C and S3, most features observed in the ground state band of both isotopologues have perpendicular $(\beta < 0)$ anisotropies at moderate kinetic energies, and isotropic $(\beta \sim 0)$ PADs for low eKEs. These features are well-reproduced by theory as shown for the 0_0 detachment spectra in Figures S6-7. However, peak I in the spectra for both isotopologues, as well as peak B in the D_2CC^- spectrum, show distinctly positive anisotropies. The shifts of peaks B and I from the vibrational origins are in excellent agreement with the values predicted by theory for detachment to the 6^1 and 5^1 neutral levels, respectively (see Table I).

The anomalous anisotropies of these regions are attributed to detachment to FC-forbidden b_2-symmetric vibrational levels activated through vibronic coupling. Let $|a\rangle$, $|b\rangle$ be two

vibronic states with vibrational symmetries $\Gamma_a^{vib}, \Gamma_b^{vib}$ and electronic symmetries $\Gamma_a^{elec}, \Gamma_b^{elec}$. These states can couple provided

$$\Gamma_a^{vib} \otimes \Gamma_b^{vib} \otimes \Gamma_a^{elec} \otimes \Gamma_b^{elec} \supset \Gamma_{TS}, \quad (0)$$

where Γ_{TS} is the totally symmetric representation in the relevant molecular point group (*47*). If only one of these states has nonzero FC-overlap with the anion ground state (i.e. $\langle anion|a\rangle = 0$, $\langle anion|b\rangle \neq 0$), then the FC-forbidden transition can appear in the photoelectron spectrum through the borrowed FC-allowed character, and its detachment characteristics (in particular, the PAD) will match those of the FC-allowed transition.

Following the *s* + *p* model developed by Sanov and co-workers (*48*), detachment from the vibrational ground state of $\tilde{X}^2B_2$ anionic vinylidene can only result in positive anisotropies if the neutral state has B_2 vibronic symmetry, suggesting that features B and I correspond to the b_2-symmetric 6^1 and 5^1 vibrational levels in $\tilde{X}^1A_1$ vinylidene ($\Gamma_{neutral}^{vib} = b_2, \Gamma_{neutral}^{elec} = A_1$). As these transitions are FC-forbidden, there must be some coupling of these states to one or more FC-allowed ($\Gamma_{neutral}^{vib} = a_1$) states which satisfies Eq. (0). Thus, the state(s) giving FC-intensity to regions B and I must be totally symmetric vibrational levels in a B_2-symmetric electronic state.

The lowest singlet vinylidene electronic state satisfying this is the $\tilde{B}^1B_2$ state, which we find to have a term energy of 3.997(3) eV in agreement with previous theoretical calculations (*26*). Detachment to this electronic state of H_2CC, shown in Figure S8, shows the same distinctly positive anisotropy observed for regions B and I in the ground state band, consistent with the assignment of the regions of anomalous anisotropies as arising from vibronic coupling to this excited state. This assignment is confirmed by the derivative coupling calculations that will be described in Section E of this document.

C. Rotational contours

a. Linewidths and rotational selection rules

In contrast to the vinylidene photoelectron spectrum of Lineberger and co-workers (*18*), the vinylidene ground state cryo-SEVI spectra do not show anomalous broadening (relative to the rotational temperatures extracted from excited state bands) for the majority of spectral features. Figure S5A compares the vibrational origins obtained for the $\tilde{X}^1A_1 \leftarrow \tilde{X}^2B_2$ band reported in the present work to those obtained for the $\tilde{A}^1A_2 \leftarrow \tilde{X}^2B_2$ transition previously reported from the Berkeley cryo-SEVI lab (*21*). A more quantitative treatment of the rotational contours is provided in the following section; as can be seen, the rotational envelopes are qualitatively similar for both electronic bands represented in Figure S5A, and this similarity indicates that detachment from rotationally cold vinylidene anions to the neutral $\tilde{X}^1A_1$ ground state does not result in features "broadened" by rapid isomerization to acetylene. Peak widths for other features in the ground state bands of both isotopologues are quite similar to the respective

origins, with the exception of FC-forbidden features in the D_2CC^- cryo-SEVI spectrum (B and I) that appear due to vibronic coupling and have substantially narrower widths (see Table I). As shown below, this difference in lineshape is a result of different rotational selection rules for these transitions.

Let l be the angular momentum of a photoelectron generated by detachment from an anion state with rovibronic symmetry $\Gamma_{rve}^{anion} = \Gamma_{rot}^{anion} \otimes \Gamma_{vib}^{anion} \otimes \Gamma_{elec}^{anion}$ to form a neutral state with symmetry $\Gamma_{rve}^{neutral}$. The general selection rule for this detachment transition is given by (*49*)

$$\Gamma_{rve}^{anion} \otimes \Gamma_{rve}^{neutral} \supset \begin{cases} \Gamma^*, l \text{ even} \\ \Gamma_{TS}, l \text{ odd} \end{cases}, \tag{0}$$

where Γ^* and Γ_{TS} are the antisymmetric and totally symmetric representations, respectively, within the relevant molecular point group. In the case of vinylidene (C_{2v}), Γ^* and Γ_{TS} are A_2 and A_1, respectively. For Franck-Condon (FC) allowed detachment from vibrationally cold $\tilde{X}^2B_2$ vinylidene anions (i.e. $\Gamma_{vib}^{neutral} = \Gamma_{vib}^{anion} = a_1$ and $\Gamma_{elec}^{anion} = B_2$), this becomes

$$\Gamma_{rot}^{anion} \otimes \Gamma_{rot}^{neutral} \otimes \Gamma_{elec}^{neutral} \supset \begin{cases} B_1, l \text{ even} \\ B_2, l \text{ odd} \end{cases} \tag{0}$$

The symmetry of the rotational wavefunction of vinylidene (an asymmetric top) is classified by the parity (even, e, or odd, o) of the two quantum numbers K_a and K_c. As addressed in the previous analysis of the vinylidene rotational contours (*21*), the cryo-SEVI resolution is only sufficient to discern rotational branches corresponding to changes in K_a due to the relative magnitudes of vinylidene's rotational constants; for H_2CC (D_2CC), $A \sim 10$ (5) cm^{-1}, whereas B, $C \sim 1$ (<1) cm^{-1} (*11, 21*). For even values of K_a, the rotational symmetry is either A_1 (K_aK_c = ee) or A_2 (eo), and for odd K_a the rotational symmetry is either B_1 (oo) or B_2 (oe) (*50*). For the FC-allowed features in the ground state band ($\Gamma_{elec}^{neutral} = A_1$), this results in the following possibilities for rotational transitions:

even l	odd l
ee ← oe	ee ← oo
eo ← oo	eo ← oe
oe ← ee	oe ← eo
oo ← eo	oo ← ee

Regardless of l, the selection rule requires that K_a must change in parity (odd ΔK_a) for FC-allowed transitions in the $\tilde{X}^1A_1 \leftarrow \tilde{X}^2B_2$ electronic band.

For a near-prolate rotor, $\Delta K_a = 0, \pm 1$ transitions are expected to dominate the rotational profile, depending on the specific electronic states involved. Thus, we take the rotational selection rule for FC-allowed transitions in the ground state band to be $\Delta K_a = \pm 1$. The low temperatures extracted from the previous vinylidene rotational contours suggests that the vast

majority of anions will occupy the lowest rotational level allowed by their nuclear spin state (*ortho*, *o*, or *para*, *p*); following the requirement that the total internal wavefunction must be antisymmetric (symmetric) upon hydrogen (deuterium) interchange, *o*-H_2CC^- (*p*-D_2CC^-) is restricted to even K_a, whereas *p*-H_2CC^- (*o*-D_2CC^-) is restricted to odd K_a. Thus, the majority of anions are in the $K_a = 0$ (*o*-H_2CC^-, *p*-D_2CC^-) or $K_a = 1$ (*p*-H_2CC^-, *o*-D_2CC^-) states, and the rotational envelopes for FC-allowed transitions will be dominated by the $1 \leftarrow 0$ and $0,2 \leftarrow 1$ transitions, which appear as three separate peaks spaced by ~$2A$. The relative intensities of these transitions are governed by nuclear spin statistics analogous to those of H_2 (D_2), which in the present case imply a 3:1 (1:2) ratio of the $K_a = 0$:$K_a = 1$ population for H_2CC^- (D_2CC^-). Since most of the H_2CC^- anions are in their $K_a = 0$ level, the single $1 \leftarrow 0$ branch dominates, whereas for D_2CC^- the $0 \leftarrow 1$ and $2 \leftarrow 1$ transitions are both prominent, resulting in a broader rotational profile for D_2CC as observed in Figure S5A.

As discussed in the main text, several features (B and I) in the ground-state band of the D_2CC^- spectrum are FC-forbidden but vibronically-allowed via coupling to the high-lying $\tilde{B}^2B_2$ excited state. The rotational selection rules for these features are based on the borrowed B_2 electronic character of these vibrational levels, and so deviate from those described above. Detachment to a B_2 electronic state results in the following possibilities for rotational transitions:

even l	odd l
ee ← ee	ee ← eo
eo ← eo	eo ← ee
oe ← oe	oe ← oo
oo ← oo	oo ← oe

Thus, regardless of l , symmetry requires an even change in K_a, so $\Delta K_a = 0$ transitions dominate the rotational profile. From the above considerations of anion temperature and nuclear spin statistics, the two expected rotational transitions are $0 \leftarrow 0$ and $1 \leftarrow 1$, which have the same energy to within <1 cm^{-1}, resulting in a single rotational branch. For D_2CC, this is the source of the narrower observed peaks for transitions B and I. This difference is illustrated in Figure S5B, which shows peaks A and B from the D_2CC^- cryo-SEVI spectrum.

b. <u>Rotational fits for the vibrational origins</u>

A more quantitative analysis of the rotational lineshapes of peak A for both isotopologues was carried out by fitting the rotational contours using the PGOPHER software (*51*). This program calculates the full rotational spectrum for excitation of a state characterized by rotational temperature *T* to a final state with excitation energy *E*; in this case, the initial and final states are the anion and neutral vibrational ground states of vinylidene. The resultant stick spectrum is convoluted with a Gaussian function of width *w*. Rotational constants (see Table S2 for values used) and vibronic symmetries for both states are specified, as are the point group of the molecule and the statistical weighting of ee/eo versus oo/oe rotational levels.

The fit results are shown as red dashed lines in Figure S5. The agreement with experiment is generally good, particularly for the H_2CC isotopologue, and gives a temperature of 17.0(6) K for H_2CC^- in reasonable agreement with from the results from a similar analysis of the excited state bands (*21*). The excitation energy from the fitting procedure give an electron affinity of

0.4866(8) eV for this isotopologue, where the uncertainty is given by the full-width at half-maximum (fwhm) of the Gaussian convolution. This is an order-of-magnitude improvement in accuracy as compared to the EA obtained by Ervin and co-workers (*18*) – 0.490(6) eV – whose error bars correspond to the instrumental resolution of their experiment.

For the deuterated isotopologue, the extracted excitation energy gives an electron affinity of 0.488(2) eV for D_2CC. The convolution width and ion temperature parameters yielded by the fitting procedure – 14(1) cm^{-1} and 27(2) K, respectively – are larger than is typically expected for the cryo-SEVI technique. This suggests a minimal amount of broadening (<1 meV) relative to the excited state band; given the lack of acetylene character in the calculated wavefunction for the 0^0 level of D_2CC, we take the source of this to be experimental in nature.

The most likely source of the relatively large fitted ion temperature is rf heating of ions in the octupole trap, which results in incomplete thermalization of the ions with the buffer gas (*52*). This is particularly an issue when operating with a large amount of ions in the trap, leading to space-charge effects which push ions towards regions where the effective potential is nonzero. While efforts were taken to tune source conditions and ion optics such that the trap was not overloaded, this often introduced great instability in the ion signal and, due to time limits imposed by the expense of the deuterated precursor (C_2D_4), some compromise needed to be made – particularly for the high-resolution scans of peak A, where detachment signal was at a minimum. Thus, it is entirely possible that the scans represented in the high-resolution peak A trace in Figure 2A correspond to detachment from ions that were not fully thermalized in the ion trap.

Working with large ion signals introduces the potential for too many detachment events with a single laser shot, which can cause anomalous broadening of peaks in the spectrum due to the inability of the centroiding algorithm to distinguish between electron events which overlap on the phosphor screen. However, this issue can always be mediated by decreasing the laser power, and so is not expected to contribute to the lineshape of the band origin in the D_2CC^- cryo-SEVI spectra.

D. Quantum dynamics calculations

The quantum dynamics calculations described here must treat both the acetylene and vinylidene isomers, and thus careful consideration is necessary to ensure that an optimal coordinate system is used. The bond-length/bond-angle Hamiltonian has a complex kinetic energy operator, which is difficult to handle numerically. While preserving atomic permutation symmetry, the HH-CC Jacobi coordinates are optimal for neither acetylene nor vinylidene. The (2+1) Radau-Jacobi coordinates used in our previous work (*24*) are optimal for vinylidene, but not for acetylene, and cannot take advantage of the permutation symmetry in the system. Hence, the calculations reported here use the CH-CH Jacobi coordinate system, which preserves the CH-CH permutation symmetry. It is optimal for acetylene, but not quite so for vinylidene. As a result, a large basis/grid is still required to cover both isomers, which makes the computation quite demanding, especially for D_2C_2.

The CH-CH Jacobi coordinates are denoted as ($r_0, r_1, r_2, \theta_1, \theta_2, \phi$). As shown in Figure 1 in the main text, r_0 is distance between the centers-of-mass of the two CH moieties, r_1 and r_2 are the two C-H bond lengths, θ_1 (θ_2) is the angle between vectors $\vec{r}_1$ ($\vec{r}_2$) and $\vec{r}_0$, and ϕ is the relative dihedral angle between the $\vec{r}_1$ and $\vec{r}_2$ vectors. The rotationless (J=0) Hamiltonian in the diatom-diatom Jacobi coordinate system is given as follows ($\mathrm{h} = 1$):

$$\hat{H} = \sum_{i=0}^{2}\left(-\frac{1}{2\mu_i}\frac{\partial^2}{\partial r_i^2}\right) + \sum_{i=0}^{2}\frac{\hat{j}_i^2}{2\mu_i r_i^2} + V(r_0, r_1, r_2, \theta_1, \theta_2, \phi), \tag{0}$$

where μ_0=(m_C+m_H)/2, μ_1=μ_2=$m_H m_C$/(m_H+m_C), $\hat{j}_1$ and $\hat{j}_2$ are the angular momentum operators for r_1 and r_2, respectively, and $\hat{j}_0^2 = (\hat{j}_1 + \hat{j}_2)^2$. V is the potential energy function developed by Han, Li, and Guo (*12*). The coordinates and Hamiltonian are defined analogously for D_2C_2 by replacing the H atoms in H_2C_2 with deuterium.

The Hamiltonian is discretized using a mixed grid-basis representation. The radial coordinates r_1 and r_2 are represented by DVR (discrete variable representation) grids and r_0 by PODVR (potential optimized DVR) (*53*), while the angular degrees of freedom are expressed in terms of associated Legendre functions. The real Chebyshev propagation is used to determine the energy levels and the wavefunctions (*54*):

$$\Psi_k = 2\hat{H}_s\Psi_{k-1} - \Psi_{k-2}, \quad k \geq 2 \tag{0}$$

with $\Psi_1 = \hat{H}_s\Psi_0$ and $\Psi_0 = \Psi_i$. The Hamiltonian in Eq. (0) was scaled to the spectral range of (-1,1) via $\hat{H}_s = (\hat{H} - H^+)/H^-$. The spectral medium and half width ($H^{\pm} = (H_{\max} \pm H_{\min})/2$) are determined by the spectral extrema, $H_{\max}$ and $H_{\min}$, which can be estimated easily from the discretized Hamiltonian. The initial wave packets (Ψ_i) on the neutral PES are anion vibrational eigenfunctions assuming photodetachment to be a vertical transition (Condon approximation). The anion wavefunctions are obtained by diagonalizing the Hamiltonian in Eq. (0) using the Lanczos method on the anion PES (*24*). In order to preserve the CH-CH permutation symmetry, the initial wave packets were symmetrized by exchanging the $\vec{r}_1$ and $\vec{r}_2$ vectors (*55*). A large basis set (8×10^8 for H_2CC and 2×10^9 for D_2CC) and a relatively long propagation (20,000 Chebyshev steps) are used to obtain convergent energy levels for both isomers (with an uncertainty of 2.0 cm^{-1}). The parameters used in the calculations are listed in Table S3.

The energy spectrum is obtained from the discrete cosine Fourier transform of the Chebyshev autocorrelation functions, $C_k \equiv \langle \Psi_0 | \Psi_k \rangle$ (*56*):

$$S(E) = \frac{1}{\pi H^- \sin\vartheta}\sum_{k=0}(2 - \delta_{k,0})\cos(k\vartheta)C_k, \tag{0}$$

where ϑ=arccos(E_s) is the Chebyshev angle, k is the Chebyshev order, and E_s is the scaled total energy corresponding to $\hat{H}_s$. Once the eigenvalues are determined, the corresponding eigenfunctions can be regenerated by rerunning the same propagation. For each eigenfunction, the assignment of vibrational quanta is based on inspecting the nodal structure of the wavefunction. Finally, the HCCH (or DCCD) weight is determined approximately by integrating the squared wavefunction in the range where both θ_1 and θ_2 are larger than 85^o or are less than 60^o. The other details of the calculations can be found in our previous work (*24*).

The calculated photoelectron spectra for detachment from the 5_1 state of H_2CC^- and D_2CC^- are shown in Figures S6 and S7, respectively. Photodetachment of this b_2 state of the anion leads to excitation of several b_2 vibrational states of the neutral vinylidene and their assignments are given in the figures. It is clear that the 5^1 and 1^16^1 states are quite close in energy for both isotopologues, consistent with the resonance formed by these two states.

In Figure S10, the 0^0, 6^2, and 5^1 wavefunctions of D_2CC are plotted in both the D_2CC and DCCD regions. Comparing with the analogous wavefunctions in Figure 3 of the main text, it is clear that deuteration significantly reduces the mixing with DCCD (see the vinylidene weights in Table I in main text). This is not surprising as the wavefunctions of deuterated vinylidene are much narrower, thus it is more difficult to access the isomerization barrier. The extent of mixing is however expected to rise with energy, leading to more significant mixing between the two isomers for vibrationally excited D_2CC.

In Figures S9 and S11, the 6^1, 3^1, 2^1, and 1^16^1 wavefunctions of H_2CC and D_2CC are presented. The smaller acetylene component in the D_2CC wavefunctions as compared to those of H_2CC is quite apparent, consistent with the calculated vinylidene weights listed in Table I. In addition, it is readily seen that the 1^16^1 wavefunction of H_2CC has a similar shape to that of the 5^1 state, suggesting significant mixing due to accidental near-degeneracy of the two states. Indeed, the energy difference between the two states is quite small (104 cm^{-1} for H_2CC). This near degeneracy suggests a large intermodal anharmonicity ($x_{1,6}$) because the harmonic value of the 1^16^1 state is 133 cm^{-1} higher than its actual energy. Coupling between the in-plane rocking and stretching is plausible due to the low isomerization barrier and the resultant large anharmonicity along the isomerization minimum energy path (*12*). The mixing is much less severe for D_2CC, evidenced by the clear and regular nodal structures of the two wavefunctions. Finally, the acetylene states that mix with the vinylidene states are of the local bender nature, which possess large number of nodes along the two angular coordinates (θ_1 and θ_2), suggesting that only the highly excited local bending states of acetylene are involved in the mixing of the two isomers This is consistent with previous theoretical analysis of the acetylene vibrational spectrum (*15*, *57, 58*).

E. Theoretical treatment of derivative coupling

In order to determine the derivative coupling between the ground and excited electronic states of vinylidene, *ab initio* calculations employing correlation-consistent polarized valence triple zeta (cc-pVTZ) basis sets on carbon and hydrogen with diffuse *s*(0.044020), *p*(0.035690),

and *d*(0.100000) functions added to carbon were performed. Molecular orbitals were optimized in a state-averaged multiconfiguration self-consistent field (SA-MCSCF) procedure averaging the four lowest states of a 2-orbital doubly-occupied space and a 7-orbital, 10-electron (all valence electron) active space. Energies and derivative couplings were computed at the multireference configuration single and double configuration interaction (MRSDCI) level, an expansion which adds to the SA-MCSCF reference space all single and double excitations out of that space. The MRSDCI expansion comprised 5,114,424 configuration state functions (CSFs). All calculations were performed using the COLUMBUS electronic structure suite (*59*).

The derivative coupling vector, given by

$$f_{Q_\alpha}^{i,j}(\mathbf{R}) = \left\langle \Psi_i(\mathbf{r};\mathbf{R}) \left| \frac{\partial}{\partial Q_\alpha} \right| \Psi_j(\mathbf{r};\mathbf{R}) \right\rangle_{\mathbf{r}}, \tag{0}$$

was evaluated using analytic gradient techniques (*60-62*). Here, Ψ_i and Ψ_j are the electronic wavefunctions of adiabatic states *i* and *j*, **R** and **r** represent nuclear and electronic coordinates, respectively, and Q_α the α internal coordinate. For the case at hand, where nuclear configurations with C_{2v} symmetry are considered, $f_{Q_\alpha}^{i,j}(\mathbf{R})$ is nonzero provided the direct product of the irreducible representation carried by states Ψ_i ($^1A_1$) and Ψ_j ($^1B_2$) and nuclear coordinate Q_α is A_1. Thus, $\left\langle \Psi_i(\mathbf{r};\mathbf{R}) \left| \frac{\partial}{\partial Q_\alpha} \right| \Psi_j(\mathbf{r};\mathbf{R}) \right\rangle_{\mathbf{r}}$ is nonvanishing for b_2 vibrations, Q_5 (antisymmetric CH stretch) and Q_6 (in-plane rock) of vinylidene. When $\mathbf{f}^{i,j}$ is computed for vinylidene, $f_{Q_6}^{i,j} = -4.080516$ is nearly 30 times larger in magnitude than $f_{Q_5}^{i,j} = 0.14426998$ and composes almost 100% of the derivative coupling vector $\left(\left\|\mathbf{f}^{i,j}\right\| = 4.08304976\right)$; therefore, states Ψ_i ($^1A_1$) and Ψ_j ($^1B_2$) are strongly coupled by the in-plane rocking mode, ν_6.

Figure S12A shows the derivative coupling vector $\mathbf{f}^{i,j}$. The top panel of Figure S12B is a plot of the $^1A_1$ and $^1B_2$ states and their mean energy along the Q_6 coordinate. The bottom panel plots the differences of states $^1A_1$ and $^1B_2$ from the mean energy.

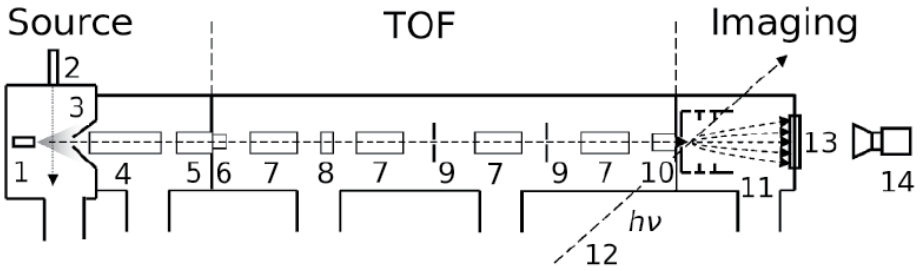

Figure S1. Schematic of the HR-PEI VMI spectrometer, segregated into three regions, as indicated. Ions are formed by a pulsed supersonic jet and pulsed discharge source (1) coupled to an electron gun (2). The resultant ion beam is skimmed (3) and passes through ion electrostatic acceleration optics (4) which direct anions to the gating, potential referencing, and bunching unit (5). The time-of-flight (TOF) region contains a number of ion optics which serve to steer and focus the beam, including two sets of electrostatic ion-beam deflectors (6, 8), an ion-beam Einzel lens (7), and stainless steel apertures (9). A potential referencing switch, electrostatic ion-beam deflectors and potential barrier (10) direct the ions into the interaction region of a VMI lens (11), where they are photodetached by a vertically-polarized laser beam (12). The resultant photoelectrons are velocity-mapped onto a 75mm multichannel plate and phosphor detector (13), which is photographed by a CCD camera (14) with each laser shot.

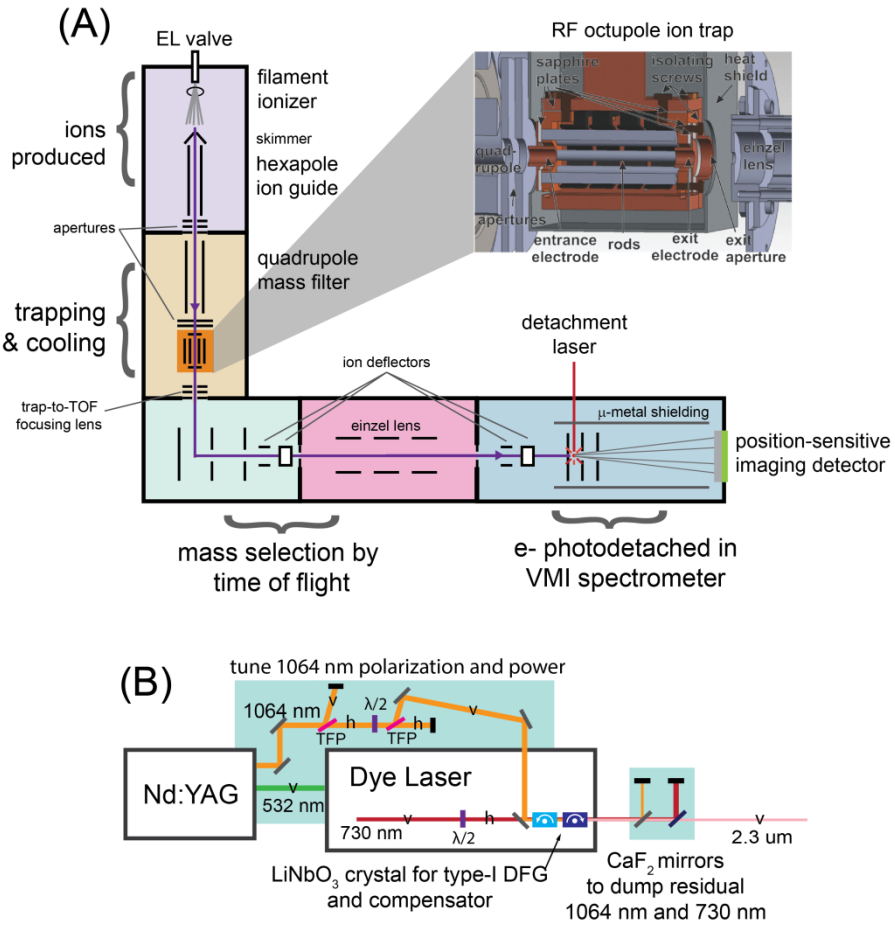

Figure S2. **A.** A schematic of the cryo-SEVI machine showing the different portions of the experiment. Each color block represents a separate differentially-pumped region. The cross-section of the radiofrequency octupole trap is reproduced from reference (*23*). **B**. The IR-DFG setup used to obtain the high-resolution traces in the vinylidene photoelectron spectrum. Vertically, horizontally, and circularly polarized light are indicated with **v**, **h**, and **c**, respectively. TFP = thin film polarizer, λ/2 = half-wave plate.

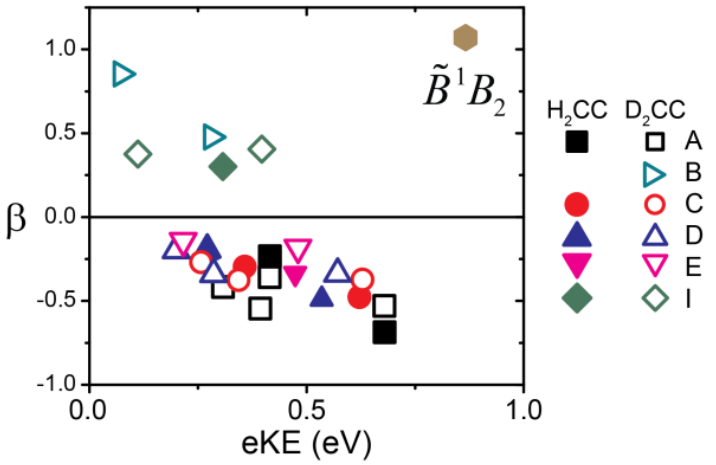

Figure S3. Photoelectron angular distributions of various features in the cryo-SEVI spectra of H_2CC^- (solid markers) and D_2CC^- (hollow markers), along with the β value calculated for detachment to the $\tilde{B}^1B_2$ neutral state of H_2CC.

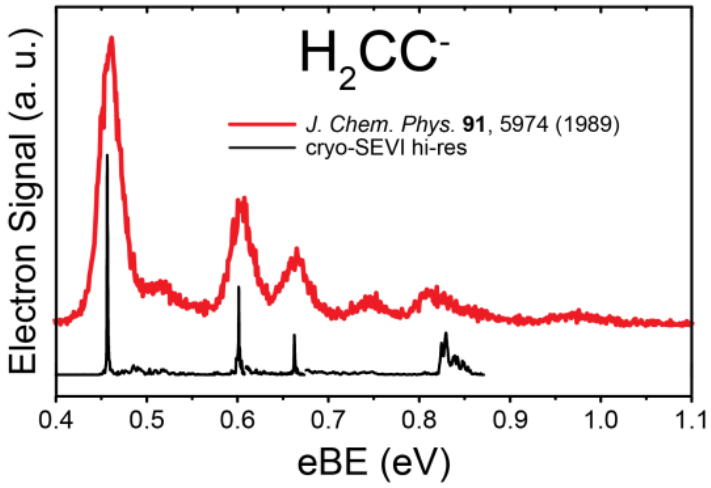

Figure S4. Comparison of the high-resolution cryo-SEVI spectrum of H_2CC^- (black) with the anion photoelectron spectrum reported previously (red) (*18*).

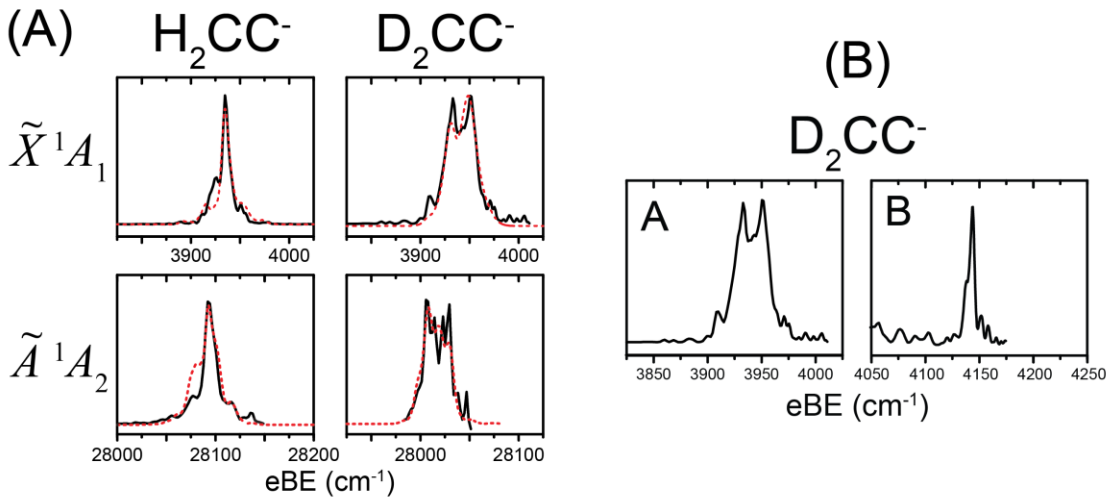

Figure S5. **A.** Comparison of rotational contours for the band origins in the $\tilde{X}^1A_1 \leftarrow \tilde{X}^2B_2$ and $\tilde{A}^1A_2 \leftarrow \tilde{X}^2B_2$ electronic bands in the cryo-SEVI vinylidene spectra. The red traces show fit rotational contours described in Section C for the $\tilde{X}^1A_1$ band and Ref. (*21*) for the $\tilde{A}^1A_2$ band. **B.** Comparison of the lineshape of peak A (0_0^0) to peak B (6_0^1) in the cryo-SEVI spectrum of D_2CC^-.

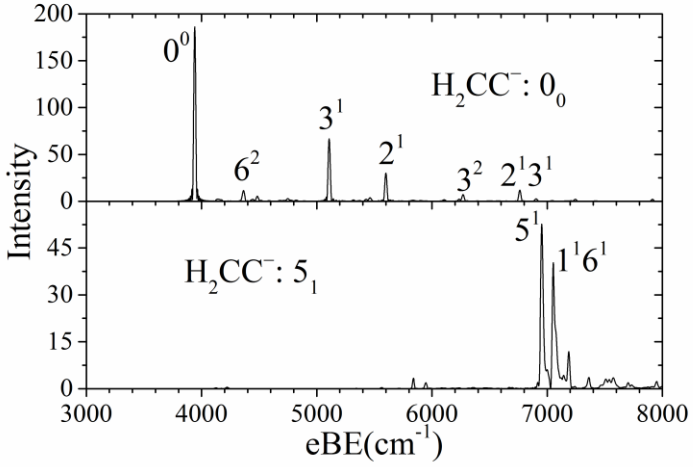

Figure S6. Calculated photoelectron spectra for detachment from the 0_0 (top) and 5_1 (bottom) states of H_2CC^- to various vibrational levels of neutral H_2CC.

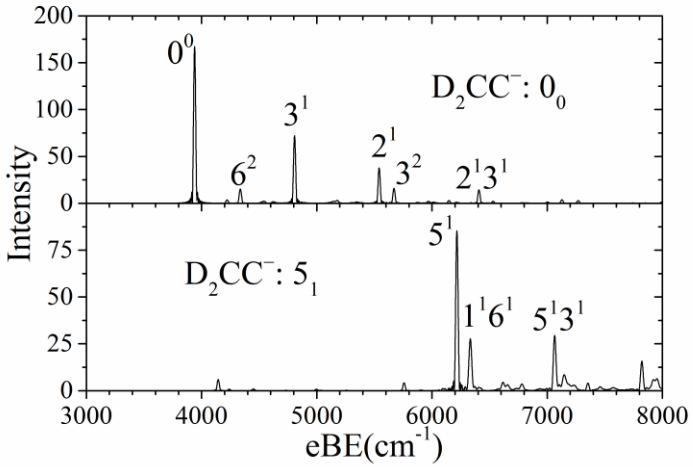

Figure S7. Calculated photoelectron spectra for detachment from the 0_0 (top) and 5_1 (bottom) states of D_2CC^- to various vibrational levels of neutral D_2CC.

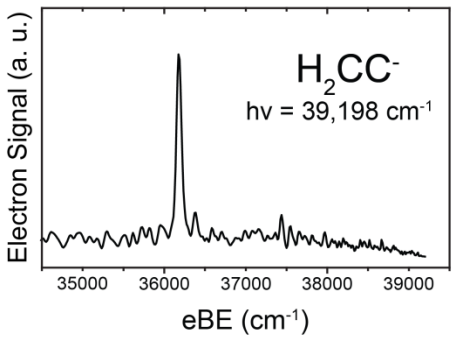

Figure S8. Photoelectron spectrum of H_2CC^- obtained from the cryo-SEVI experiment showing detachment to the $\tilde{B}^2B_2$ excited neutral state.

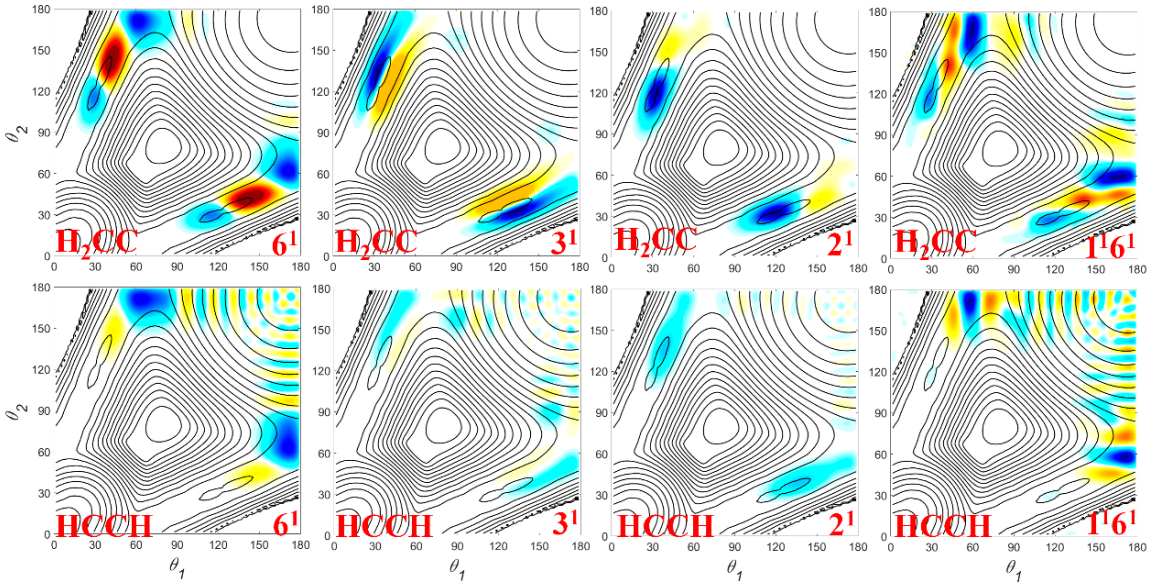

Figure S9. Wavefunctions of the 6^1, 3^1, 2^1, and 1^16^1 states of H_2CC.

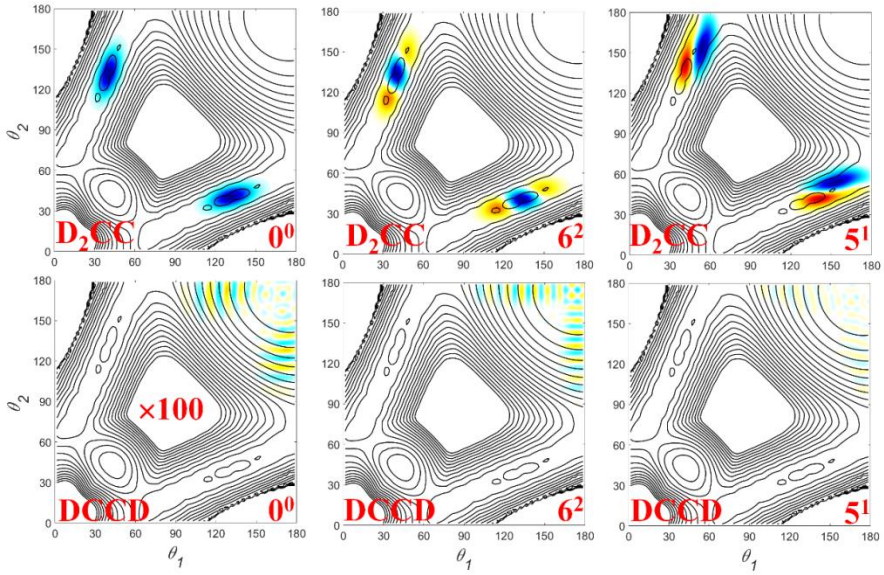

Figure S10. Wavefunctions of the 0^0, 6^2, and 5^1 states of D_2CC.

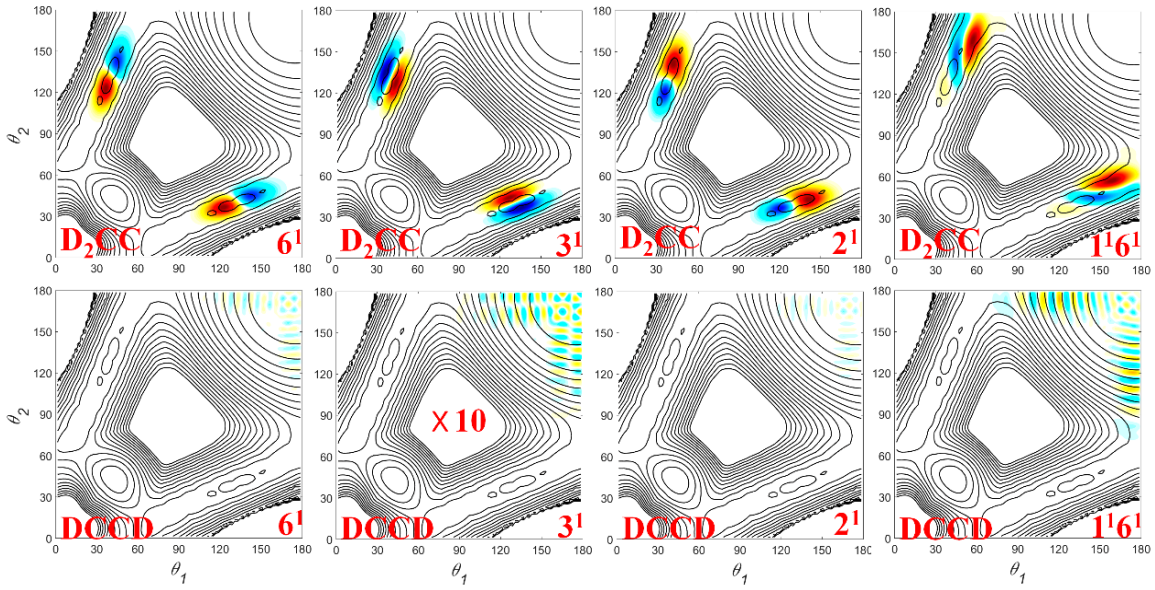

Figure S11. Wavefunctions of the 6^1, 3^1, 2^1, and 1^16^1 states of D_2CC.

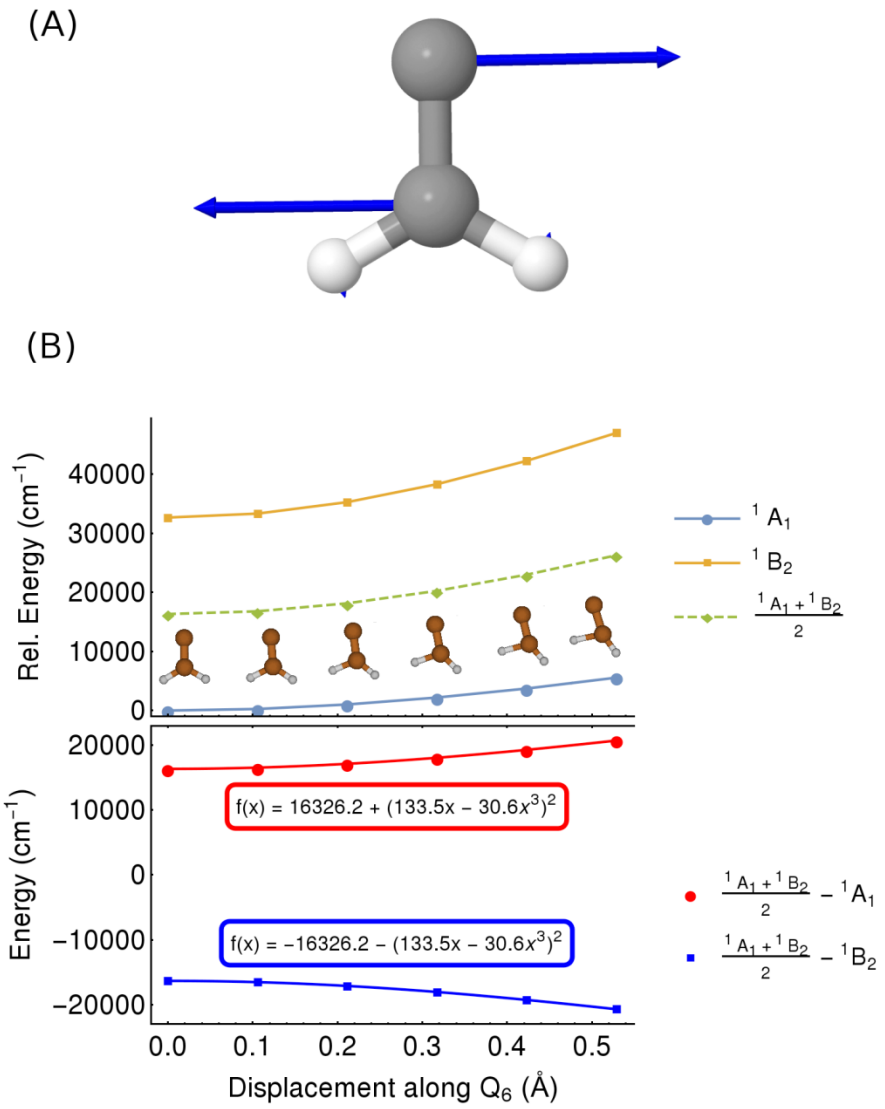

Figure S12. A. Vector representation of the derivative coupling between $^1A_1$ and $^1B_2$, $\mathbf{f}^{1,3}$. **B.** (Top) plot of $^1A_1$ and $^1B_2$ state energies and their mean along the in-plane rocking mode, Q_6. (Bottom) plot of the deviation of each state from the mean energy. The $H_2CC \rightarrow HCCH$ transition state is located 0.913 Å along the Q_6 mode and features an electronic (ZPE-adjusted) barrier of 1639.5 (1005.8) cm^{-1}.

Table S1. Binding energies, peak widths, and shifts from the origin of features a-e underlying region I in the cryo-SEVI spectrum of H_2CC^-.

Peak	eBE (cm^{-1})	fwhm (cm^{-1})	shift from A (cm^{-1})
a	6904	16	2966
b	6943	35	3005
c	7018	11	3080
d	7045	32	3107
e	7097	19	3159

Table S2. Rotational constants (in cm^{-1}) for the anion and neutral ground states of H_2CC and D_2CC. The constants for neutral D_2CC were obtained using the equilibrium geometry for neutral H_2CC reported in Ref. (*12*).

	anion		neutral	
	H_2CC^- (*21*)	D_2CC^- (*21*)	H_2CC (*11*)	D_2CC
A	9.9227	4.9652	9.5318	4.7502
B	1.2166	1.0236	1.3338	1.1221
C	1.0837	0.8486	1.1573	0.9077

Table S3. Numerical parameters (in a. u.) used in wave packet calculations.

	HC--CH	DC--CD
Grid/basis ranges and sizes	$r_1, r_2 \in (1.42, 5.78)$ $N_1 = N_2 = 26$	$r_1, r_2 \in (1.42, 5.78)$ $N_1 = N_2 = 28$
	$r_0 \in (0.8, 3.2)$ $N_0 = 22$	$r_0 \in (1.35, 3.0)$ $N_0 = 35$
Largest values of j_1, j_2 and m	38, 38, 38	42, 42, 42
Propagation steps	20,000	20,000